coatings

MDPI

Article

Intentionally Incorporated Fe Cations in Silverton Polyoxometalates Forming Fenton-like Photocatalysts for Enhanced Degradation

Hongmei Dong [1], Di Gao [2], Baoyi Li [1], Hongdao Li [1], Lifeng Ding [1,*] and Yulan Niu [1,*]

[1] Department of Chemistry and Chemical Engineering, Taiyuan Institute of Technology, Taiyuan 030008, China; lefdhm831221@163.com (H.D.)
[2] College of Chemistry and Chemical Engineering, Chongqing University, Chongqing 400044, China
* Correspondence: dinglf@tit.edu.cn (L.D.); niuyl@tit.edu.cn (Y.N.)

Abstract: Polyoxometalates (POMs) have shown great potential for applications in photocatalysis due to their unique structural features, tunable band gap, and environmental benignity. Herein, a Fe ion-incorporated $Co_4W_6O_{21}(OH)_2{\cdot}4H_2O$ sphere network POM was successfully synthesized via a simple hydrothermal process. A DFT calculation proved that the Fe ion partially replaced cobalt atoms, forming $Fe_xCo_{4-x}WOH$, which played a crucial role in modulating the electron state and the band structure. The as-prepared $Fe_xCo_{4-x}WOH$ exhibited excellent Fenton-like photocatalytic activity; the degradation rate of RhB improved 3.69 times compared with the sample without doping. The favorable performance of $Fe_xCo_{4-x}WOH$ is a result of the synergistic effects of the Fenton reaction and the activation of H_2O_2 under visible irradiation, which can generate a mass of $\bullet O_2^-$ and •OH species in the unique sphere network structure. This study supplied a new idea for designing highly-active Fenton-like POM photocatalysts for environmental remediation.

Keywords: polyoxometalates; $Fe_xCo_{4-x}WOH$; hydrothermal; Fenton-like photocatalytic



Citation: Dong, H.; Gao, D.; Li, B.; Li, H.; Ding, L.; Niu, Y. Intentionally Incorporated Fe Cations in Silverton Polyoxometalates Forming Fenton-like Photocatalysts for Enhanced Degradation. *Coatings* **2023**, *13*, 1084. https://doi.org/10.3390/coatings13061084

Academic Editor: Emerson Coy

Received: 6 May 2023
Revised: 4 June 2023
Accepted: 9 June 2023
Published: 12 June 2023



Copyright: © 2023 by the authors. Licensee MDPI, Basel, Switzerland. This article is an open access article distributed under the terms and conditions of the Creative Commons Attribution (CC BY) license (https://creativecommons.org/licenses/by/4.0/).

1. Introduction

In recent years, it has been reported that combining a photoinduced reaction with other advanced oxidation processes (AOPs) can increase the yield of oxidation products and thus improve catalytic efficiency [1,2]. The Fenton reaction is one of the important AOPs reactions, which has been widely used in sewage treatment. The combination of Fenton chemistry and light irradiation, with its high reactivity and non-selectivity of the hydroxyl radical (HO•), has become a highly efficient oxidation technology, which can greatly promote the decomposition of toxic degraded organic pollutants in wastewater [3–8]. Some high-performance photocatalysts for Fenton photodegradation, such as $WO_3/ZnFe_2O_4/BiOBr$, Fe-based MOFs, C/Fe-Mn-O, etc. [9–11], have been developed during the past years.

Polyoxometalates (POMs) based on transition metals have been considered as promising photocatalysts because of their unique structural features, low cost, tunable band gap, and environmental benignity. Iron-containing POMs have been investigated for the fabrication of Fenton-like photocatalysts for degradation pollutants by some research groups. For example, An et al. reported the use of Keggin-type phosphotungstate POM/TiO_2 Fenton-like photocatalysts with rearranged oxygen vacancies to promote synergetic degradation. Compared with the pristine TiO_2, the synergistic degradation activity of a Fenton photocatalyst for toxic dye and 5-Sulfosalicylic acid was increased by 5 times and 3.5 times, respectively. This improvement was ascribed to the excellent effect of oxygen vacancy regulation in activating oxygen and H_2O_2 molecules to form $\bullet O_2^-$ and •OH radicals [12]. Therefore, in the view of materials science, iron-containing POMs are proper candidates for designing AOPs-based functional photocatalysts.

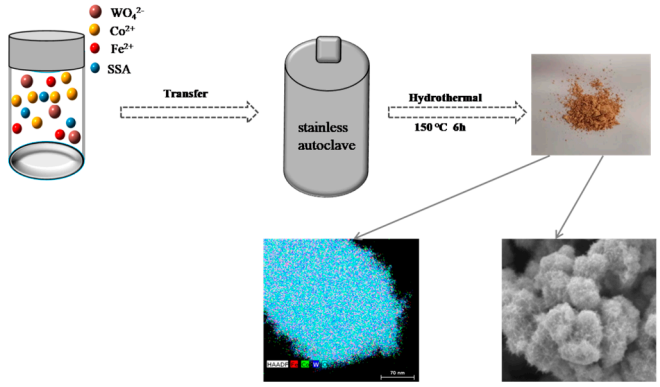
Recently, we reported on original 3D framework $Co_4W_6O_{21}(OH)_2{\cdot}4H_2O$ (denoted as CoWOH) microstructures for the first time. The XRD analysis revealed that the polyoxoanion had a Silverton structure, which contained six $\{W_2O_9\}$ units connected at the angle forming an $\{X\text{-}O_{12}\}$ icosahedron and three types of Co coordination. The ion radius of Fe is close to that of the Co cation, which is favorable for its substitution at the Co site. The Fe element has a different number of 3d electrons and can regulate the electronic structure of POMs. Moreover, the electron configuration of Fe^{2+} is $3d^6$, which is suitable for octahedral or tetrahedral positions, while the electron configuration of Co cations is $3d^{6-8}$, which is conducive to octahedral coordination, according to the stable energy of the crystal field [13,14]. We predict that replacing Co cations with the iron element could introduce a Fenton reaction for the Co-based POMs and improve their photocatalytic performance.

With this in mind, we fabricated Fe^{2+} doping Silverton-type CoWOH nanomaterials via an in situ hydrothermal self-assembly route. Considering the similar ion radius and electronic orbit of Fe and Co, we speculate that the Fe element can occupy parts of the sites of cobalt in six coordination to form $Fe_xCo_{4-x}WOH$. The effect of Fe incorporation on the chemical formation energy and structure of CoWOH is investigated for the first time. Its mechanistic and photocatalytic properties were studied in detail. Therefore, this report provides some valuable ideas for the development and research of new materials as Fenton reagents.

2. Experimental Section

2.1. Materials Preparation

$Fe_{2.1}Co_{1.9}W_6O_{21}(OH)_2{\cdot}4H_2O$ (called FeCoWOH-3) was synthesized via the facile hydrothermal method with the assistance of SSA (Scheme 1). In a typical process, $FeCl_2{\cdot}6H_2O$, $CoCl_2{\cdot}6H_2O$, and 0.6597g sodium tungstate dihydrate ($Na_2WO_4{\cdot}2H_2O$) were added into 20 mL deionized (DI) water with vigorous stirring to form a transparent solution at room temperature. The mole feed ratio of Fe and Co is 1:3, and the total molar amounts remain at 2 mmol. After that, 2 mmol of 5-sulfosalicylic acid (SSA) was dissolved in the mixture solution. Afterwards, the uniform brick-red solution was transferred to a stainless autoclave and heated at 150 °C for 6 h. Then, the resulting Murrey precipitates were washed several times, alternately with deionized water and anhydrous ethanol, and dried for 5 h at 70 °C under vacuumed conditions. All the used chemicals were provided by Chuan Dong Ltd., Chongqing, China (analytical grade) and could be used without further purification.



Scheme 1. The synthesis of FeCoWOH-3 in Fe:Co = 1:3 at 159 °C for 6 h via a facile hydrothermal route.

2.2. Characterization

The as-prepared samples were analyzed via an X-ray diffraction system (XRD, Shimadzu ZD-3AX, Kyoto, Japan). The morphologies of the precipitates were examined via scanning electron microscopy (SEM, Nova 400 Nano-SEM, FEI, Hillsboro, OR, USA) and high-resolution transmission electron microscopy (HRTEM, Titan G2 60–300, FEI, Hillsboro, OR, USA) with an EDX detector. The structure and surface components of the materials

were measured using a Fourier transform infrared spectrometer (FTIR, Magna-IR-750, Thermo Fisher Scientific, Waltham, MA, USA), and X-ray photoelectron spectroscopy (XPS, Escalab, 250Xi, Al Kα, Thermo Fisher Scientific, Waltham, MA, USA). UV–vis diffuse reflectance spectra were obtained for the dry-pressed disk samples via a TU-1900 recording spectrophotometer, and the Shimadzu ICPS-7500 spectrometer was adopted to conduct inductively coupled plasma–atomic emission spectroscopy (ICP-AES, Kyoto, Japan) analysis. Electron spin resonance (ESR, Bruker, Billerica, MA, USA) tests were performed using a Bruker A300 spectrometer.

2.3. Photo-Assisted Fenton-like Degradation of Pollutants

The photocatalytic measurement was performed using the previously reported method [14]. A 300W Xe lamp (PLS-SXE 500, CEAULIGHT Beijing, Beijing, China) with a 420 nm cutoff filter (420 nm < λ < 760 nm) was used as the light source (light intensity 50 mW cm^{-2}). Typically, the photocatalyst (20 mg) was dispersed into 40 mL Rhodamine B (RhB) (20 mg/mL) aqueous solution under a 300 W Xe lamp (as modeling sunlight) at 298 K. Before photocatalytic experiment, the test solution was stirred in the dark for about 30 min to achieve a stable equilibrium between adsorption and desorption. Changes in RhB concentration were determined via a UV–vis spectrophotometer (TU-1901, Beijing, China).

2.4. Recycling Performance of the FeCoWOH-3 Photocatalyst as Photocatalyst

After degradation, the catalysts were collected by filtration, whereas the photocatalytic activity of the composites did not deteriorate significantly even after four consecutive cycles, indicating the extraordinary stability of the synthesized samples, as displayed in Figure S5 in the Supporting Information.

3. Results and Discussion

3.1. Characterization of the Obtained Samples

The crystal structures of CoWOH and FeCoWOH-3 were measured via X-ray diffraction (XRD). As shown in Figure 1a, all of the diffraction peaks can be well indexed as the orthorhombic structure of CoWOH (JCPDS 47-0142). However, the incorporation of Fe atoms introduced some detectable peaks, where the two peaks are marked with black stars. These wide diffraction peaks may come from the substrate or other amorphous matter, which has little effect on our whole structure. The partial enlarged XRD spectra are shown in Figure 1b. To further understand the influence of Fe doping on the structure of CoWOH, we performed a Rietveld refinement for FeCoWOH-3 samples using a GSAS program (Figure 1c). The results demonstrate that Fe atoms were successfully doped in CoWOH. The FeCoWOH-3 sample maintains the cubic structure of CoWOH with the space group of *Im3*. The doped Fe atoms mainly occupy Co sites, owing to their similar ionic radius and electronic orbit. The morphologies of CoWOH and FeCoWOH-3 were characterized via SEM and TEM. As shown in Figures 2a and S1a,b, the CoWOH sample shows sphere networks composed by nanobelt self-assembly (Figure 2a), exhibiting a uniform diameter of several hundred nanometers (Figure 2b). After incorporating Fe atoms, the size of the sphere become slightly larger compared to the undoped CoWOH sphere (Figure 2c,d). The morphology of the samples was further explored using TEM images (Figures 2e and S1c,d). For FeCoWOH-3 in Figure 2e, the average diameter of the individual nanobelt was about 8 nm. The SAED patterns of FeCoWOH-3 are shown in Figure 2f, which display several white rings, revealing the polycrystal nature of the FeCoWOH-3 sample. In addition, the N_2 adsorption/desorption isotherms test was employed to estimate the Brunauer–Emmett–Teller (BET) specific surface area of the CoWOH and FeCoWOH-3 samples (Figure S2). Obviously, the surface area increased from 66.725 m^2/g for CoWOH to 108.420 m^2/g for FeCoWOH-3. Generally speaking, the larger the specific surface area of the catalyst, the higher the catalytic efficiency. This is because the active sites of the catalyst are mainly distributed on its surface. The larger the specific surface area is, the more active sites there are. The more active sites there are on the surface of the catalyst, the easier it is to activate

the molecules, and the greater the area of contact between the reactants and the catalyst, the faster the reaction. This demonstrates that the doping iron atoms replace some of the cobalt atoms, distort the crystal lattice (as shown in Figure S3), and alter the structure of the catalyst's pores; thus, they increase the specific surface area of the catalyst [15]. It is well known that surface area often plays a critical role in improving the photocatalytic properties. In order to investigate its surface, FeCoWOH-3 microspheres were investigated using EDX mapping (Figure 3f), and the results demonstrated that the Fe, Co, O, and W elements were uniformly distributed on the surface of the sample. Further, the inductively coupled plasma atomic emission spectroscopy (ICP-AES; see Table S1 in the Supporting Information) was used to quantify the contents and proportions of Co, Fe, and W. The analysis shows the sum of the formula $Fe_{2.1}Co_{1.9}W_6O_{21}(OH)_2{\cdot}4H_2O$, which is approximately consistent with the feed ratio of Co: Fe = 3:1 in the precursor.

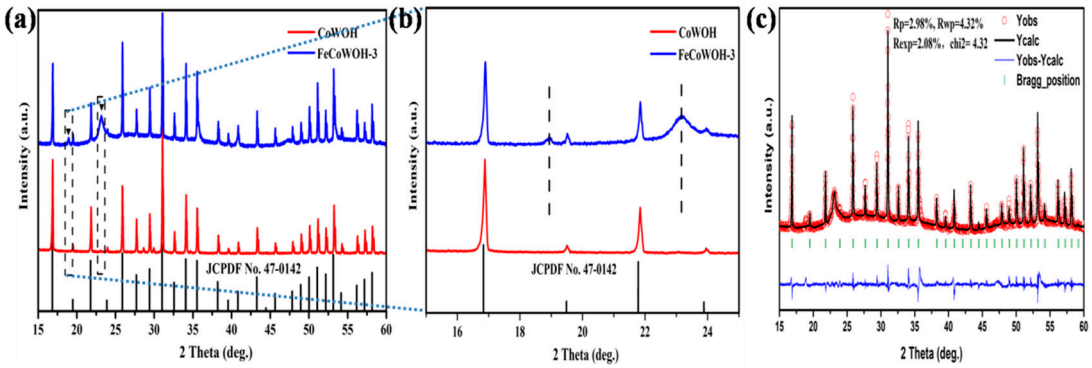


Figure 1. (**a**) XRD patterns of CoWOH and FeCoWOH-3 samples. (**b**) Partial enlarged XRD spectra. (**c**) Experimental neutron powder diffraction pattern and Rietveld refinement for FeCoWOH-3 with Co/Fe feed ratio of 1:3.

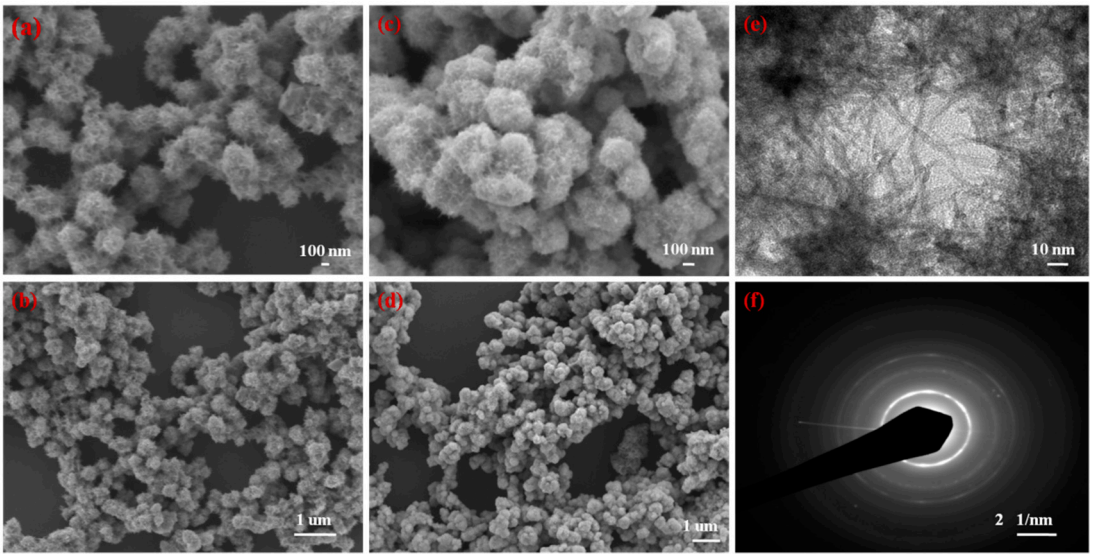


Figure 2. (**a**,**b**) Typical SEM images of CoWOH; (**c**,**d**) FeCoWOH-3 samples; (**e**) HRTEM images of FeCoWOH-3; (**f**) the SAED pattern of the FeCoWOH-3.

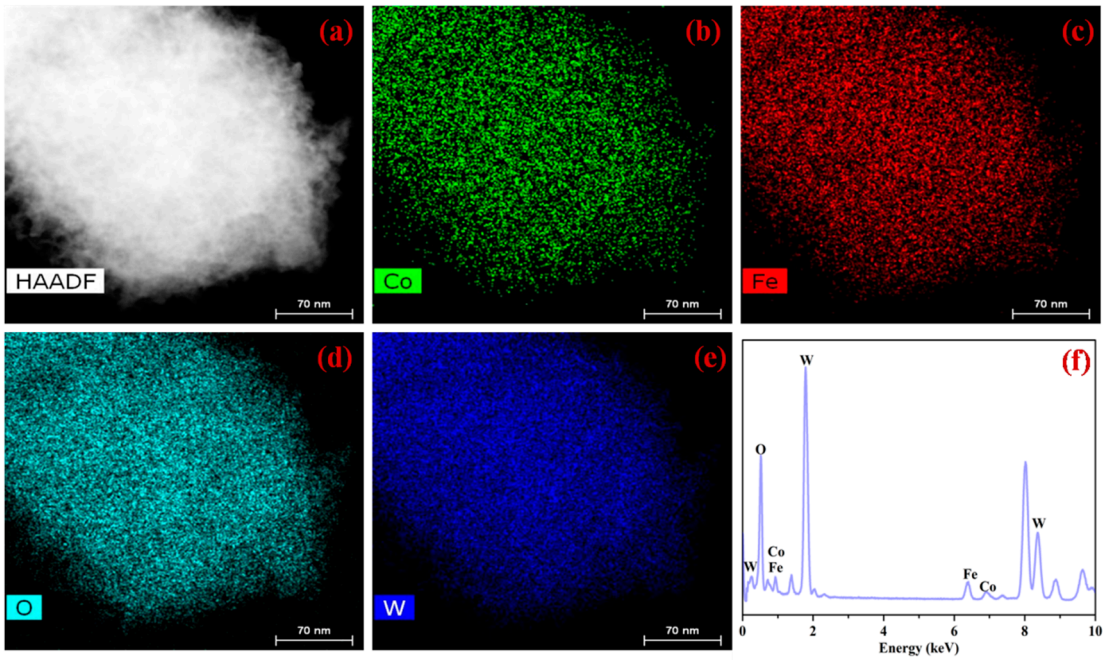


Figure 3. HRTEM-EDX elemental mapping of the FeCoWOH-3. (**a**) HAADF; (**b**) Co element; (**c**) Fe element; (**d**) O element; (**e**) W element; (**f**) EDX mapping.

The XPS measurement was conducted to investigate the surface chemical states and electronic structure of the materials. The appearance of C 1s is due to the inevitable adsorption of hydrocarbons on the surface of FeCoWOH-3 microcrystals [16,17]. The high-resolution XPS spectra of Co 2p, Fe 2p, W 4f, and O 1s of the obtained samples are shown in Figure 4a–d. The Co 2p spectrum consists of spin-orbit split $2p_{3/2}$ and $2p_{1/2}$ components (Figure 4a) with the same chemical information [18]. Hence, only the higher-intensity Co $2p_{3/2}$ peak and corresponding satellite peak were analyzed. A sharp peak observed at 780.9 eV is related to the existence of Co $2p_{3/2}$ and a broad satellite peak is located at 786.1 eV. The appearance of a broad and prominent satellite peak demonstrates the typical Co^{2+} oxidation state. Figure 4b displays the XPS spectrum of the two main peaks of Fe 2p (Fe $2p_{3/2}$ and $Fe2p_{1/2}$). The peaks at 710.8 eV and 724.0 eV belonged to the Fe^{2+}, while the peaks at 726.0 eV and 713.2 eV together with the shakeup satellites (716.2 eV) demonstrated the presence of Fe^{3+} on the surface. The presence of the Fe(III) peak was inevitable during the preparation of a compound containing iron [19]. Moreover, Figure 4c presents the O 1s XPS spectrum which can be divided into three characteristic components, denoted as O1, O2, and O3, respectively. The O1 peak at 533.2 eV can be attributed to the adsorption of H_2O or H_2O near the surface [20,21]. The O2 peak at 531.2 eV is assigned to the oxygen in the OH^- groups of $Co_4W_6O_{21}(OH)_2{\cdot}4H_2O$, and the O3 peak at 530.5 eV belongs to the lattice oxygen species of (O^{2-}) [21–23]. At the binding energies of 37.6 eV and 35.4 eV, the W 4f core-level spectrum (Figure 4d) shows the spin doublets W $4f_{5/2}$ and W $4f_{7/2}$, respectively, demonstrating the existence of W^{6+} species on the surface [24].

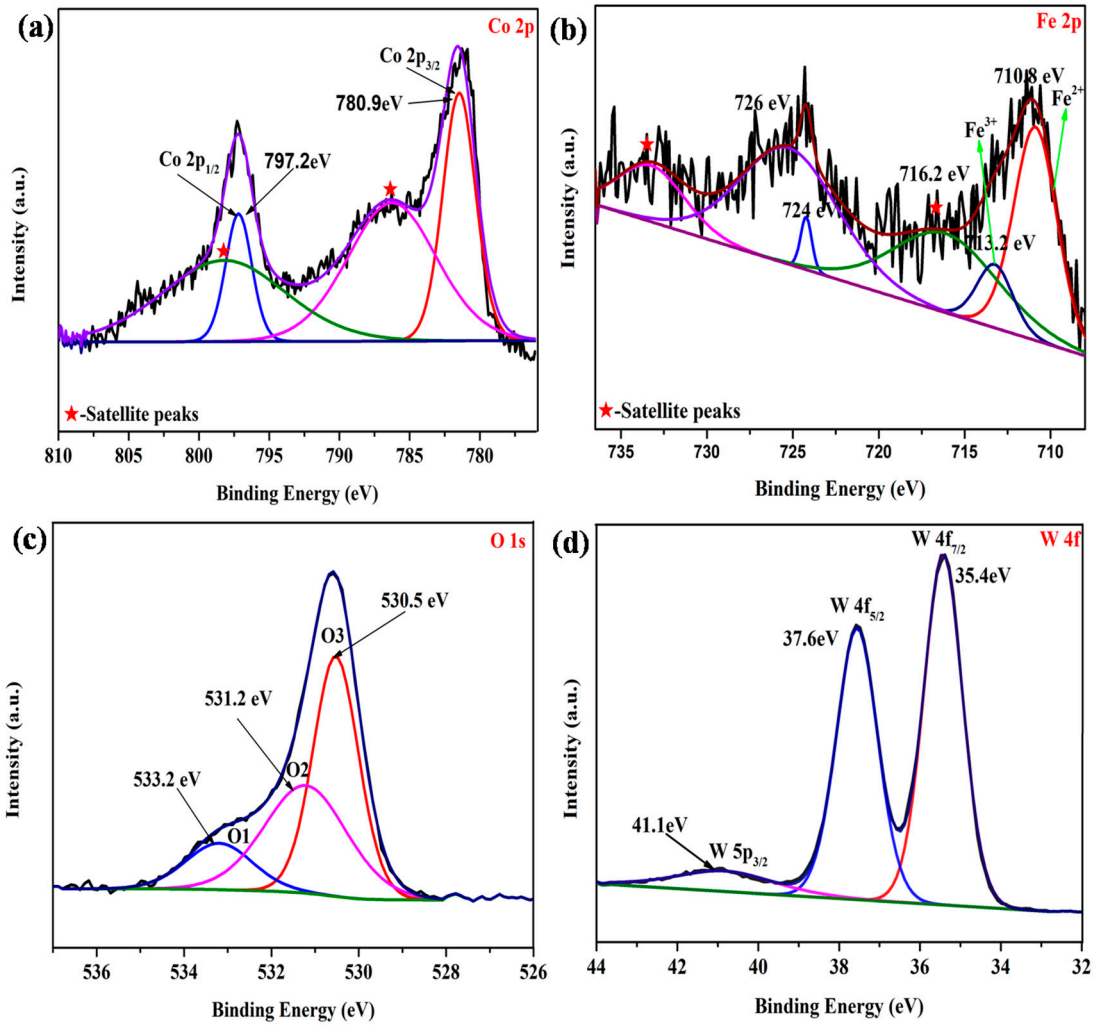


Figure 4. XPS analysis of prepared FeCoWOH-3, (**a**) Co 2p, (**b**) Fe 2p, (**c**) O 1s, (**d**) W 4f.

Further, we used a theoretical calculation to illustrate the formation energy during the incorporated processing of metal cations in the $Fe_xCo_{4-x}WOH$. Density functional theory (DFT)-optimized crystal structures of CoWOH are shown in Figure 5a; the polyoxoanion has a Silverton structure, which contains twenty four $\{WO_6\}$ groups. In the volume phase, two $\{WO_6\}$ octahedrons are connected coplanar to form $\{W_2O_9\}$ units, and six $\{W_2O_9\}$ units are connected at the angle to form an $\{X\text{-}O_{12}\}$ icosahedron. In addition, there are two types of Co coordination, where one is coordinated by six O forming $\{CoO_6\}$ octahedral, and the other is surrounded by ten O atoms forming $\{CoO_{10}\}$, and the third is surrounded by twelve O atoms forming $\{CoO_{12}\}$. All oxygen atoms belong to one of three kinds of chemical environments: the first oxygen atoms belong to the bridging oxygen atoms within the $\{W_2O_9\}$ unit, the second oxygen atoms belong to the bridging oxygen atoms between the {CoOx} unit and $\{WO_6\}$, and the third oxygen atoms are the bridging oxygen atoms between the {CoOx} unit and {CoOx}. Figure 5b displays the Wyckoff position of the cobalt atoms in the CoWOH, which shows three different occupying situations for cobalt atoms. "2a" is the cobalt atom at the vertex, "6b" is the cobalt atom at the $\{CoO_{10}\}$ unit, and "8c" is the cobalt atom at the $\{CoO_6\}$ unit. The preface also mentioned that the radius of the Fe ion is similar to that of the Co ion, which makes it favorable for iron to replace Co. In addition, the electron configuration of Fe^{2+} is $3d^6$, suitable for octahedral, while the electron configuration of Co cations is $3d^{6-8}$. So, we calculated the formation energies of iron at different sites, as shown in Figure 5c. The calculated results show that the formation energy is the lowest at the Wyckoff position of "8c", indicating that iron preferentially

replaces cobalt atoms at octahedral sites. Then, we calculated again the formation energies of different precursor concentrations of iron at octahedral sites. The results show that the most stable formation energy occurs when the ratio of iron to cobalt is equal (Figure 5d). This is consistent with the ratio of iron to cobalt in the final sample, which is close to 1:1. In addition, from the perspective of crystal engineering, it has been reported that the hybrid degree of the transition metal 3d orbital and oxygen 2p orbital is stronger after doping iron, and the energy band center of these two orbitals is closer, which provides a stronger driving force for oxygen exchange between the catalyst surface and adsorption groups [25]. We will demonstrate later that the successful sites' elective incorporation of Fe benefits the enhancement of the photocatalytic activity of CoWOH.

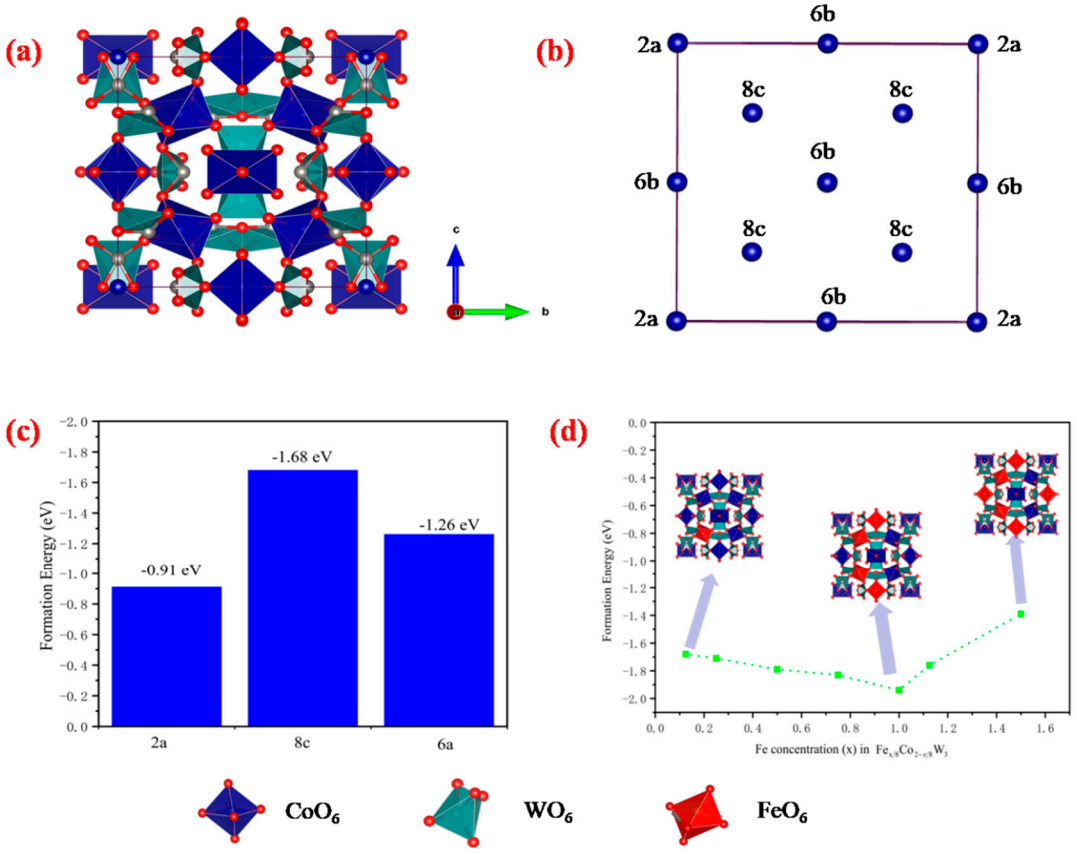


Figure 5. (**a**) The structure of CoWOH; (**b**) the Wyckoff position of the cobalt atoms in the CoWOH; (**c**) the formation energy of iron in each Wyckoff position; (**d**) the relationship between formation energy and Fe proportions in FeCoWOH.

The FeCoWOH-3 hierarchical microspheres were tested via FT-IR spectroscopy to characterize functional groups (Figure 6a). The strong absorption peaks located in the range of 400–1000 cm^{-1} are indicated for the vibrational mode peaks of the Co-O, W-O, and W-O-W bonds, respectively. The result suggests that the structure of FeCoWOH-3 is similar to that of CoWOH. The peaks at 850 cm^{-1} and 668 cm^{-1} are related to the O-W-O and W-O bonds, respectively. The obvious peak that appeared at 1650 cm^{-1} indicates the existence of the O-H stretching vibration mode of water molecules. In addition, the weak band at 1468 cm^{-1} belongs to the H-O-H bond of adsorbed water [26–28]. To further verify the optical absorption properties of samples, the UV–vis diffuse reflection spectroscopy was measured (Figure 6b). The absorption edge of CoWOH is about 562 nm because of the intrinsic transition. According to the mathematical relationship between absorption wavelength and band gap, E(eV) = 1240/λ(nm), the calculated optical gap is 2.21 eV. After the doped Fe element, the absorption peak shows a blue-shift, and the absorption edge of FeCoWOH-3 is about 540 nm. Similarly, the band gap is about 2.30 eV. However, the

visible light absorption of the FeCoWOH-3 is enhanced in contrast to the pure CoWOH. The UV–vis spectral results further indicate that the doping of the Fe ion changes the electron state and the band structure of CoWOH.

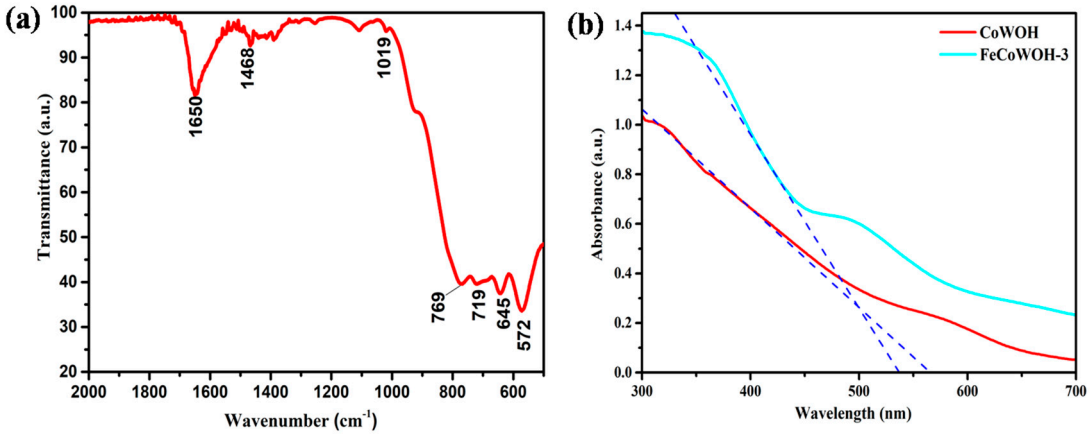


Figure 6. (**a**) FT-IR spectrum curve of FeCoWOH-3. (**b**) UV–vis absorption spectra of CoWOH and FeCoWOH-3.

3.2. Photodegradation of RhB

The visible-light photocatalytic degradation of RhB was selected as a model to verify the photocatalytic activity of FeCoWOH-3. The absorption spectrum of the degradation process of 40mL RhB solution (added 0.6mL H_2O_2) via FeCoWOH-3 is shown in Figure 7a. The spectrogram showed that the absorption peak of RhB solution completely disappeared after 25 min, which demonstrated the excellent photocatalytic performance of the FeCoWOH-3 microstructures. The XRD patterns of FeCoWOH-3 samples after the reaction are provided in Figure S6. The XRD data show that the structure of our sample remains basically unchanged after the reaction, which further indicates the stability of its structure. In addition, we have made a performance comparison with similar materials in the same industry. Table S2 of the table showing the support materials further indicates the excellent performance of our materials. Moreover, $Fe_{2.1}Co_{1.9}W_6O_{21}(OH)_2{\cdot}4H_2O$ presents a 3.69 times enhanced degradation rate of RhB compared with the pristine sample; such a large improvement is ascribed to the unique sphere network structure and the Fenton-like catalyst mechanism, which can not only react with Fe species to generate hydroxyl radicals, but can also capture photogenerated electrons quickly and improve photoinduced carrier separation in the presence of H_2O_2. Even though the addition of H_2O_2 in the photocatalytic system enhanced the activity of TiO_2, it can be seen from the different curves in Figure 7b that the removal effect of TiO_2 on the dye is still unsatisfactory. Therefore, the coexistence of FeCoWOH-3 and H_2O_2 significantly improved the catalytic performance, indicating that there was a synergistic effect between photocatalysis and hetero-Fenton-like reactions. It also demonstrates the great potential of Fenton-like photocatalysts.

In addition, in order to have a basic understanding of the mechanism of Fenton-like photocatalysis, experiments were carried out to capture different active substances. Isopropanol (IPA), ethylene diaminetetra acetic acid disodium salt (EDTA-2Na), and benzoquinone (BQ) were applied to inhibit the activities of hydroxyl radicals (•OH), holes (h^+), and superoxide radicals ($\bullet O_2^-$), respectively [29–31]. In Figure 7c, we exhibit the active species trapping tests of the FeCoWOH-3 photocatalyst in the degradation process of RhB. Based on the introduction of BQ, the photocatalytic activity showed a significant decline, indicating that $\bullet O_2^-$ was the main active substance in the RhB degradation process. The addition of IPA presented a certain inhibitory effect on the degradation of RhB, proving that OH has a moderate effect. In contrast, the RhB degradation was almost unchanged after the addition of EDTA-2Na in the solution. Therefore, $\bullet O_2^-$ and •OH can be considered as the main species of RhB degradation by FeCoWOH-3 materials, especially $\bullet O_2^-$, as shown in

Scheme 2. The generation of $\bullet O_2^-$ and •OH, with the presence of FeCoWOH-3, was further detected by the electron spin resonance (ESR) instrument. As shown in Figure 8a, six typical signals were detected in methanol solution when the sample was exposed to visible light, and compared with the dark state, the light intensity increases obviously, indicating that $\bullet O_2^-$ is formed during this process. Meanwhile, similar results are observed in Figure 8b. Hence, a stronger ESR signal of •OH was found on the surface of FeCoWOH-3. Based on the above experiments, the possible reaction steps in the photocatalytic RhB degradation process of RhB can be summarized as follows:

$$\text{FeCoWOH-3} + h\nu = \text{FeCoWOH-3}\ (e^- + h^+) \quad (1)$$

$$Fe^{2+} + H_2O_2 \rightarrow Fe^{3+} + HO^- + \bullet OH \quad (2)$$

$$H_2O_2 + \bullet OH \leftrightarrow HOO\bullet + H_2O \quad (3)$$

$$HOO\bullet \rightarrow H^+ + \bullet O_2^- \quad (4)$$

$$2HOO\bullet \rightarrow H_2O + O_2 \quad (5)$$

$$Fe^{3+} + H_2O_2 \rightarrow Fe^{2+} + H^+ + HOO\bullet \quad (6)$$

$$Fe^{3+} + HOO\bullet \rightarrow Fe^{2+} + H^+ + O_2 \quad (7)$$

$$RhB + \bullet O_2^- + \bullet OH \rightarrow \text{other products} \rightarrow CO_2 + H_2O \quad (8)$$

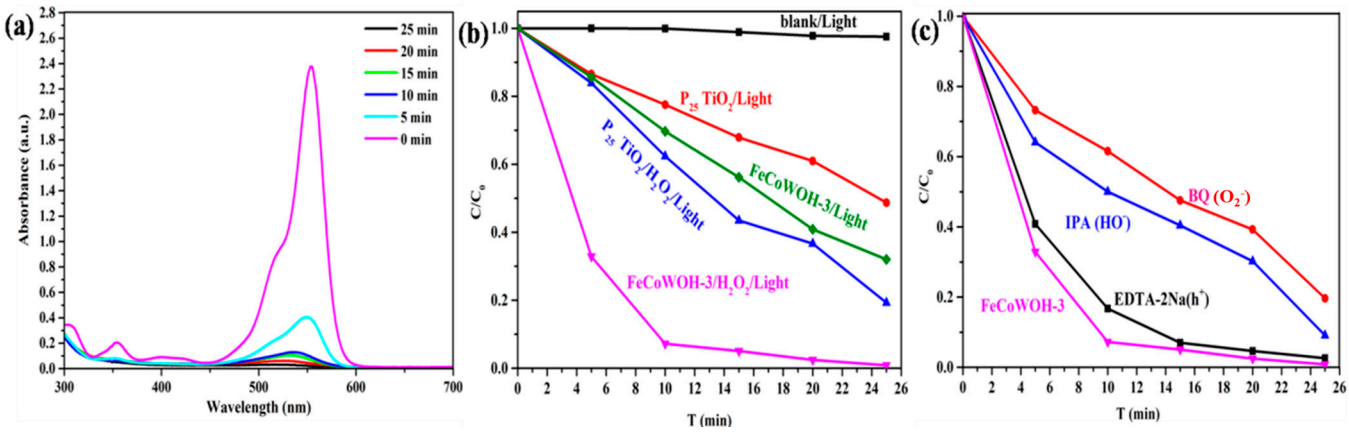
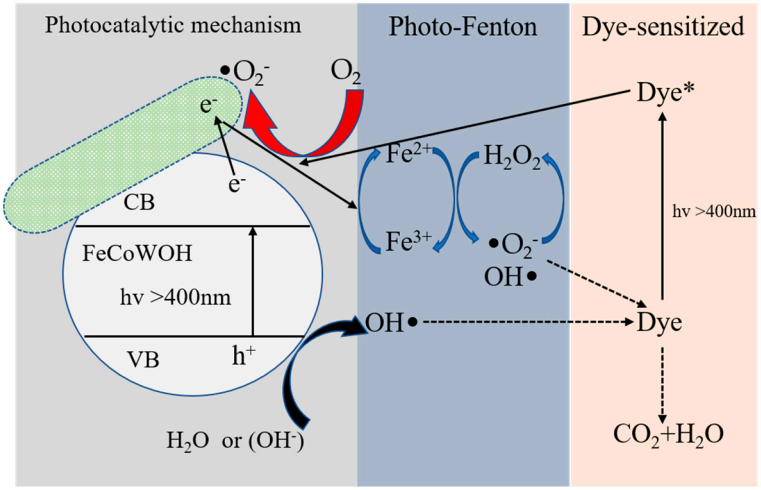


Figure 7. (**a**) Absorption spectra and (**b**) comparison of different catalytic reactions for degradation of RhB dyes. (**c**) Active species trapping experiments of FeCoWOH-3 catalyst under visible-light irradiation.

Except for the pure Fenton reaction, the amounts of hydrogen peroxide for the degradation of RhB dyes without a catalyst under visible-light irradiation were determined, as shown in Figure S4. When the hydrogen peroxide concentration is lower than 0.25%, the increase in hydrogen peroxide concentration leads to the increase in hydroxyl. It promotes the forward progression of the above Equations (3)–(5). When the concentration of hydrogen peroxide is higher than 12.5%, the excess hydrogen peroxide cannot produce more free radicals through decomposition, but quickly oxidizes Fe^{2+} to Fe^{3+} at the beginning of the reaction, thus consuming hydrogen peroxide and inhibiting the production of hydroxyl.



Scheme 2. Band diagram and mechanism of charge separation and migration for FeCoWOH.

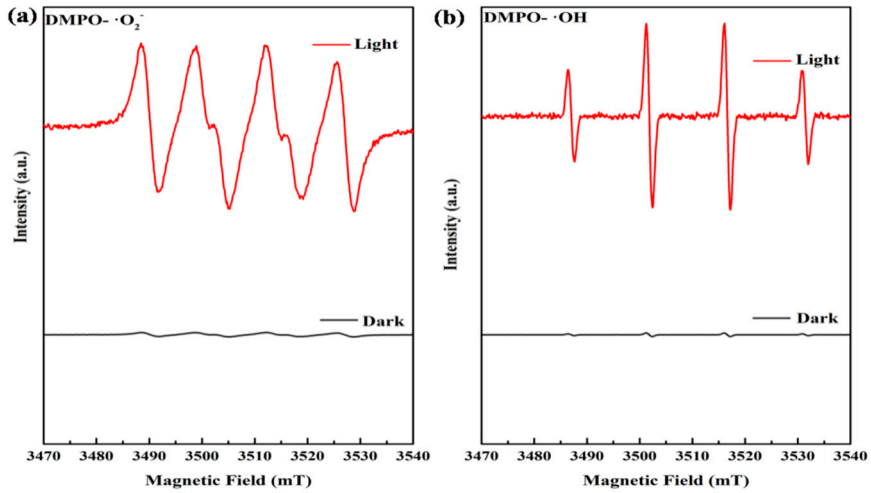


Figure 8. (**a**) ESR spectra of DMPO-•O_2^- adducts in aqueous solution over FeCoWOH-3; (**b**) ESR spectra of DMPO-•OH adducts in aqueous solution over FeCoWOH-3.

4. Conclusions

In summary, the Fe ion incorporated cobalt-POM with a hollow sphere structure has been successfully synthesized through a facile self-assembly hydrothermal strategy, and it was used as an efficient Fenton-like photodegradation catalyst. Our theoretical calculations show that Fe ions tend to be located at octahedral points, which can further adjust the electronic structure of $Fe_xCo_{4-x}WOH$ and the band gap. Its excellent photocatalytic activity is ascribed to the synergistic effects of the Fenton reaction and the activating H_2O_2 under visible irradiation, which can generate a mass of •O_2^- and •OH species in the unique sphere network structure. The current results provide new insights into the Fenton-like POMs that can effectively promote the activation processes of coexisting Fe species and H_2O_2, and pave the way for new methods for the design and synthesis of high-performance, easily-obtained enhanced photodegradation materials.

Supplementary Materials: The following supporting information can be downloaded at https://www.mdpi.com/article/10.3390/coatings13061084/s1, Table S1: Metal content quantification by ICP-AES (wt.-%); Figure S1: (a,b) TEM images of CoWOH samples; (c,d) TEM images of FeCoWOH-3 samples; Figure S2: Nitrogen adsorption-desorption isotherms for as-obtained the CoWOH and FeCoWOH-3 samples; Figure S3: (a) HRTEM images of CoWOHsamples; (b) HRTEM images of FeCoWOH-3 samples; Figure S4: Comparison of different volume ratio of hydrogen peroxide for degradation RhB dyes without catalyst under visible-light irradiation; Figure S5: Cycling experiments for the degradation of RhB over FeCoWOH; Figure S6: XRD patterns of FeCoWOH-3 samples after the reaction; Table S2: Comparison of photocatalytic properties of different similar materials.

Author Contributions: H.D.: Writing—Original draft and Characterization analysis. D.G., H.L. and B.L.: Characterization analysis and reviewing. L.D. and Y.N.: Review and editing. All authors have read and agreed to the published version of the manuscript.

Funding: This work was supported by the Scientific and Technological Innovation Programs of Higher Education Institutions in Shanxi (No. 2021L552, 2021).

Institutional Review Board Statement: Not applicable.

Informed Consent Statement: Not applicable.

Data Availability Statement: Not applicable.

Conflicts of Interest: The authors declare that there is no conflict of interest.

References

1. Leone, D.; Fendrich, M.-A.; Parrino, F.; Patel, N.; Orlandi, M.; Miotello, A. Light-Induced Advanced Oxidation Processes as PFAS Remediation Methods: A Review. *Appl. Sci.* **2021**, *11*, 8458–8484.
2. Lin, J.K.; Tian, W.J.; Zhang, H.Y.; Duan, X.G.; Sun, H.Q.; Wang, H.; Fang, Y.F.; Huang, Y.P.; Wang, S.B. Carbon nitride-based Z-scheme heterojunctions for solar-driven advanced oxidation processes. *J. Hazard. Mater.* **2022**, *434*, 128866. [CrossRef] [PubMed]
3. Cheng, X.M.; Zu, L.H.; Jiang, Y.; Shi, D.L.; Cai, X.M.; Lin, S.J.; Qin, Y. A Titanium-based Photo-Fenton Bifunctional Catalyst of mp-MXene/TiO_{2-x} Nanodots for Dramatic Enhancement of Catalytic Efficiency in Advanced Oxidation Processes. *Chem. Commun.* **2018**, *54*, 11622–11625. [CrossRef]
4. Wang, Q.J.; Cui, Y.; Huang, R.J.; Zhong, L.F.; Yan, P.; Zhang, S.L.; Zhao, Q.H.; Jiang, D.H.; Tang, A.D.; Yang, H.M. A heterogeneous Fenton reaction system of N-doped TiO_2 anchored on sepiolite activates peroxymonosulfate under visible light irradiation. *Chem. Eng. J.* **2020**, *383*, 123142. [CrossRef]
5. Yue, D.T.; Qian, X.F.; Kan, M.; Fang, M.Y.; Jia, J.P.; Yang, X.D.; Zhao, Y.X. A Metal-free Visible Light Active Photo-electro-Fenton-like Cell for Organic Pollutants Degradation. *Appl. Catal. B Environ.* **2018**, *229*, 211–217. [CrossRef]
6. Maroudas, A.; Pandis, P.K.; Chatzopoulou, A.; Davellas, L.-R.; Sourkouni, G.; Argirusis, C. Synergetic decolorization of azo dyes using ultrasounds, photocatalysis and photo-fenton reaction. *Ultrason. Sonochem.* **2021**, *71*, 105367. [CrossRef] [PubMed]
7. Yoon, M.; Oh, Y.; Hong, S.; Lee, J.S.; Boppella, R.; Kim, S.H.; Mota, F.M.; Kim, S.O.; Kim, D.H. Synergistically Enhanced Photocatalytic Activity of Graphitic Carbonnitride and WO_3 Nanohybrids Mediated by Photo-Fenton Reaction and H_2O_2. *Appl. Catal. B Environ.* **2017**, *206*, 263–270. [CrossRef]
8. Wang, N.; Du, Y.C.; Ma, W.J.; Xu, P.; Han, X.J. Rational Design and Synthesis of SnO_2-encapsulatedα-Fe_2O_3 Nanocubes as a Robust and Stable Photo-Fenton Catalyst. *Appl. Catal. B Environ.* **2017**, *210*, 23–33. [CrossRef]
9. Wang, G.W.; Cheng, H.F. Facile synthesis of a novel recyclable dual Z-scheme WO_3/$NiFe_2O_4$/BiOBr composite with broad-spectrum response and enhanced sonocatalytic performance for levofloxacin removal in aqueous solution. *Chem. Eng. J.* **2023**, *461*, 141941. [CrossRef]
10. Xia, H.; Zhang, Z.; Liu, J.; Deng, Y.; Zhang, D.X.; Du, P.Y.; Zhang, S.T.; Lu, X.Q. Novel Fe-Mn-O Nanosheets/wood Carbon Hybrid with Tunable Surface Properties as a Superior Catalyst for Fenton-like Oxidation. *Appl. Catal. B Environ.* **2019**, *259*, 118058–118069. [CrossRef]
11. Liao, X.Y.; Wang, F.; Wang, F.; Cai, Y.; Yao, Y.; Teng, B.T.; Hao, Q.L.; Lu, S.X. Synthesis of (100) Surface Oriented MIL-88A-Fe with Rod-like Structure and Its Enhanced Fenton-like Performance for Phenol Removal. *Appl. Catal. B Environ.* **2019**, *259*, 118064–118074. [CrossRef]
12. An, X.Q.; Tang, Q.W.; Lan, H.C.; Liu, H.J.; Qu, J.H. Polyoxometalates/TiO_2 Fenton-like Photocatalysts with Rearranged Oxygen Vacancies for Enhanced Synergetic Degradation. *Appl. Catal. B Environ.* **2019**, *244*, 407–413. [CrossRef]
13. Burns, R.G.; Fyfe, W.S. Site of Preference Energy and Selective Uptake of Transition-MetalIons from a Magma. *Science* **1964**, *144*, 1001–1003. [CrossRef]
14. Dong, H.M.; Li, Y.H.; Gao, D.; Zhou, M.; Hu, X.L.; Peng, H.R.; Yang, L.; He, J.; Zhang, Y.H.; Xiao, P. Efficient Self-assembly Solvothermal Synthesis of Octahedral $CuWO_4$ Microstructures Assisted by Ethylene Glycol. *J. Alloys Compd.* **2019**, *785*, 660–668. [CrossRef]

15. Yu, J.H.; Wang, G.H.; Cheng, B.; Zhou, M.H. Effects of Hydrothermal Temperature and Time on the Photocatalytic Activity and Microstructures of Bimodal Mesoporous TiO_2 Powders. *Appl. Catal. B Environ.* **2007**, *69*, 171–180. [CrossRef]
16. Rajagopal, S.; Nataraj, D.; Khyzhun, O.Y.; Djaoued, Y.; Robichaud, J.; Mangalaraj, D. Hydrothermal Synthesis and Electronic Properties of $FeWO_4$ and $CoWO_4$ Nanostructures. *J. Alloy. Compd.* **2010**, *493*, 340–345. [CrossRef]
17. Tang, Y.L.; Rong, N.N.; Liu, F.L.; Chu, M.S.; Dong, H.M.; Zhang, Y.H.; Xiao, P. Enhancement of the Photoelectrochemical Performance of $CuWO_4$ Films for Water Splitting by Hydrogen Treatment. *Appl. Surf. Sci.* **2016**, *361*, 133–140. [CrossRef]
18. Artyushkova, K.; Levendosky, S.; Atanassov, P.; Fulghum, J. XPS Structural Studies of Nano-composite Non-platinum Electrocatalysts for Polymer Electrolyte Fuel Cells. *Top. Catal.* **2007**, *46*, 263–275. [CrossRef]
19. Yang, Y.J.; Xu, L.J.; Li, W.Y.; Fan, W.J.; Song, S.; Yang, J. Adsorption and Degradation of Sulfadiazine over Nanoscale Zero-valent Ironencapsulated in Three-dimensional Graphene Network Through Oxygendriven Heterogeneous Fenton-like Reactions. *Appl. Catal. B Environ.* **2019**, *259*, 118057–118071. [CrossRef]
20. Zhu, Y.L.; Zhou, W.; Chen, Y.B.; Yu, J.; Liu, M.L.; Shao, Z.P. A High-performance Electrocatalyst for Oxygen Evolution Reaction: $LiCo_{0.8}Fe_{0.2}O_2$. *Adv. Mater.* **2015**, *27*, 7150–7155. [CrossRef]
21. Wang, Y.Y.; Ren, J.W.; Wang, Y.Q.; Zhang, F.Y.; Liu, X.H.; Guo, Y.; Lu, G.Z. Nanocasted Synthesis of Mesoporous $LaCoO_3$ Perovskite with Extremely High Surface Area and Excellent Activity in Methane Combustion. *J. Phys. Chem. C* **2008**, *112*, 15293–15298. [CrossRef]
22. Smith, R.D.L.; Prevot, M.S.; Fagan, R.D.; Trudel, S.; Berlinguette, C.P. Water Oxidation Catalysis: Electrocatalytic Response to Metal Stoichiometry in Amorphous Metal Oxide Films Containing Iron, Cobalt, and Nickel. *J. Am. Chem. Soc.* **2013**, *135*, 11580–11586. [CrossRef]
23. Roginskaya, Y.E.; Morozova, O.V.; Lubnin, E.N.; Ulitina, Y.E.; Lopukhova, G.V.; Trasatti, S. Characterization of Bulk and Surface Composition of $Co_xNi_{1-x}O_y$ Mixed Oxides for Electrocatalysis. *Langmuir* **1997**, *13*, 4621–4627. [CrossRef]
24. Penner, S.; Liu, X.J.; Klötzer, B.; Klauser, F.; Jenewein, B.; Bertel, E. The Structure and Composition of Oxidized and Reduced Tungsten Oxide Thin Films. *Thin Solid Film.* **2008**, *516*, 2829–2836. [CrossRef]
25. Liu, Y.; Yin, Y.R.; Fei, L.F.; Liu, Y.; Hu, Q.Z.; Zhang, G.G.; Pang, S.Y.; Lu, W.; Mak, C.L.; Luo, X.; et al. Valence Engineering via Selective Atomic Substitution onTetrahedral Sites in Spinel Oxide for Highly Enhanced Oxygen Evolution Catalysis. *J. Am. Chem. Soc.* **2019**, *141*, 8136–8145. [CrossRef]
26. Juliet Josephine Joy, J.; Victor Jaya, N. Structural, Magnetic and Optical Behavior of Pristine and Yb Doped $CoWO_4$ Nanostructure. *J. Mater. Sci. Mater. Electron.* **2013**, *24*, 1788–1795. [CrossRef]
27. Xu, X.W.; Shen, J.F.; Li, N.; Ye, M.X. Facile Synthesis of ReducedGraphene Oxide/$CoWO_4$ Nanocomposites with Enhanced Electrochemical Performances for Supercapacitors. *Electrochim. Acta* **2014**, *150*, 23–24. [CrossRef]
28. Naik, S.J.; Salker, A.V. Solid State Studies on Cobalt and Copper TungstatesNano Materials. *Solid State Sci.* **2010**, *12*, 2065–2072. [CrossRef]
29. Schneider, J.T.; Firak, D.S.; Ribeiro, R.R.; Zamora, P. Use of scavenger agents in heterogeneous photocatalysis: Truths, half-truths, and misinterpretations. *Phys. Chem. Chem. Phys.* **2020**, *22*, 15723–15733. [CrossRef] [PubMed]
30. Chen, Z.H.; Wang, W.L.; Zhang, Z.G.; Fang, X.M. High-efficiency Visible-light-driven Ag_3PO_4/AgI photocatalysts: Z-scheme Photocatalytic Mechanism for Their Enhanced Photocatalytic Activity. *J. Phys. Chem. C* **2013**, *117*, 19346–19352. [CrossRef]
31. Hong, Y.Z.; Jiang, Y.H.; Li, C.S.; Fan, W.Q.; Yan, X.; Yan, M.; Shi, W.D. In-situ Synthesis of Direct Solid-state Z-scheme V_2O_5/g-C_3N_4 Heterojunctions with Enhanced Visible Light Efficiency in Photocatalytic Degradation of Pollutants. *Appl. Catal. B* **2016**, *180*, 663–673. [CrossRef]

Disclaimer/Publisher's Note: The statements, opinions and data contained in all publications are solely those of the individual author(s) and contributor(s) and not of MDPI and/or the editor(s). MDPI and/or the editor(s) disclaim responsibility for any injury to people or property resulting from any ideas, methods, instructions or products referred to in the content.